Global assessment of the skills of satellite precipitation products to retrieve extreme rainfall events causing landsliding.

Odin MARC,[a] Romulo A. JUCÁ OLIVEIRA,[b] Marielle GOSSET,[a] Robert EMBERSON,[c, d, e] Jean-Philippe MALET[f]

[a] *Géosciences Environnement Toulouse (GET), UMR 5563, CNRS/IRD/CNES/UPS, Observatoire Midi-Pyrénées, Toulouse, France*

[b] *Laboratoire d'Etudes en Géophysique et Océanographie Spatiales (LEGOS), Université de Toulouse III/CNRS/CNES/IRD, Observatoire Midi-Pyrénées, Toulouse, France*

[c] *NASA Goddard Space Flight Center, Hydrological Sciences Laboratory, United States of America*

[d] *Universities Space Research Association, Columbia, MD, USA*

[e] *NASA Goddard Earth Sciences Technology and Research, Columbia, MD, USA*

[f] *Institut Terre et Environnement de Strasbourg, ITES - CNRS/UMR7063, EOST/Université de Strasbourg, 5 rue Descartes, F-67084 Strasbourg, France.*

Corresponding author: Odin Marc, odin.marc@get.omp.eu

ABSTRACT

Rainfall-induced landsliding is a global and systemic hazard, likely to increase with the projections of increased frequency of extreme precipitation with current climate change. However, our ability to understand and mitigate landslide risk is strongly limited by the availability of relevant rainfall measurements in many landslide prone areas. In the last decade, global satellite multi-sensor precipitation products (SMPPs) have been proposed as a solution but very few studies have assessed their ability to adequately characterize rainfall events triggering landsliding. Here, we address this issue by testing the rainfall pattern retrieved by 2 SMPPs (IMERG and GSMaP) and a hybrid product (MSWEP) against a large, global database of 20 comprehensive landslide inventories associated with well-identified storm events. We found that after converting total rainfall amounts to an anomaly relative to the 10-year return rainfall, R*, the three products do retrieve the largest anomaly (of the last 20 years) during the major landslide event for many cases. However, the degree of spatial collocation of R* and landsliding varies from case to case and across products, and we often retrieved R*>1 in years without reported landsliding. Additionally, the few (4) landslide events caused by short and localized storms are most often undetected. We also show that, in at least five cases, the SMPPs spatial pattern of rainfall anomaly matches landsliding less well than radar-derived rainfall amounts or lightning maps, underlining the limited accuracy of the SMPPs. We conclude on some potential avenues to improve SMPPs retrieval, and their relation to landsliding.

SIGNIFICANCE STATEMENT

Rainfall-induced landsliding is a global hazard, expected to increase as a result of anthropogenic climate change. Our ability to understand and mitigate this hazard is strongly limited by the lack of rainfall measurements in mountainous areas. Here, we perform the first global assessment of the potential of three high-resolution precipitation datasets, derived from satellite observations, to capture the rainfall characteristics of 20 storms which led to widespread landsliding. We find that accounting for past extreme rainfall statistics, most storms causing landslides are retrieved by the datasets. However, the shortest storms are often undetected, and the detailed spatial pattern of extreme rainfall appears often distorted. Our work opens new ways to study global landslide hazard but also warns against over-interpreting rainfall derived from satellites.

1. Introduction

Landsliding, broadly referring to any downslope movement of soil and rock masses, is a global hazard causing thousands of fatalities every year (Petley, 2012, Froude and Petley, 2018) and substantial economic losses. Together with shallow earthquakes, rainfall (either intense and/or prolonged; e.g. intensity vs. amounts) is the main trigger of landsliding, mainly by increasing slope pore-water pressures and reducing frictional resistance of the soil or rock masses (Wilson and Wieczoreck, 1995, Van Asch et al., 1999, Iverson, 2000). Thus, although rainfall is often required for triggering the failure, the size, location and timing of the rupture will substantially depend on various parameters such as surface and subsurface slope geometry, material strength, such as friction and cohesion, and hydrological properties such as porosity and permeability (Terzaghi, 1943, Iverson, 2000).

Since hydro-mechanical properties of rock mass and their spatial variability are hard to constrain, it is a major challenge to generalize mechanistic models for rainfall-induced landslides at anything more than local scales (Rosso et al., 2006; Baum et al., 2010, von Ruette et al., 2014), limiting the development of landslide hazard forecasting, in contrast to other hydro-meteorological hazard, such as flood forecasting (e.g., Han and Coulibaly, 2014, Wu et al., 2020). Most empirical approaches have focused on developing meteorological thresholds (e.g., rainfall intensity-duration) for quantifying landslide occurrences (e.g., Caine, 1980, Guzzetti et al., 2008). More recently, two new approaches have emerged. The first one aims at developing hydro-meteorological thresholds (Bogaard and Greco, 2018), more in phase with hydrological and mechanistic considerations on landslide triggering (Mirus et al., 2018, Thomas et al., 2018). The second approach, which focuses on relating changes in landslide density with rainfall magnitude beyond the threshold, relies on the generation of large landslide inventories (Chen et al., 2009, 2013; Saito et al., 2014, Marc et al., 2018, 2019). Importantly, such approaches based on landslide populations, and not on individual landslides, require rainfall information at the catchment scale (~100 km^2) rather than at the hillslope scale (0,001 km^2). Still, for most of these studies limitations on rainfall and/or landslide data availability are key issues.

The proliferation of medium to high resolution (<15m) satellite sensors (multi-spectral and Synthetic Aperture Radar/SAR imagery) allows researchers to detect, map and monitor landslides triggered by rainfall events in more and more settings (Marc et al., 2018, Amatya et al. 2021, Emberson et al., 2021). However, extensive gauge networks (or weather radar data) are lacking in most landslide-prone areas (e.g., Central and South-East Asia, Central and South America, Central Africa). Thus, for the last decade rainfall data retrieved from satellite constellation measurements have been considered as a potential alternative to study and potentially nowcast landslide hazard globally (Hong et al., 2007, Kirschbaum et al., 2009, Farham and AghaKouchak, 2013). This approach has recently culminated into an automatic hazard awareness system, based on daily and antecedent (seven-day) rainfall derived from satellite multisensor precipitation products (SMPP) and susceptibility maps derived from global maps of land cover, slope and distance to roads and faults (Kirschbaum et al., 2015, Kirschbaum and Stanley, 2018, Stanley et al., 2021). The key advantages of SMPP are their global coverage, and their fair spatial and temporal resolution (typically 1h, 0.1°). Still, many issues with the retrieved precipitation properties have been observed, including: (i) difficulty in capturing orographic rainfall (Aghakouchak et al., 2011, Shige et al., 2012, Yamamoto et al., 2017), (ii) difficulty in retrieving short duration and/or very intense rainfall (Mehran and AghaKouchak, 2011) or rainfall over terrain transition (e.g., coastal areas, Tan et al., 2018; You et al. 2020), (iii) generally increasing uncertainties and bias in between microwave sensor overpass (e.g., Tan et al. 2016) leading to a misrepresentation of the precipitation features, (i.e., size, shape, and orientation) affecting the location and timing of the peak rainrate (Guilloteau et al. 2021).

Currently, very few studies have quantitatively tested the ability of these products to retrieve and map extreme rainfall leading to widespread landsliding. In Italy, several SMPPs have been tested to derive rainfall threshold for landslide and debris flow triggering (Nikolopoulos et al., 2017, Rossi et al., 2017, Brunetti et al., 2018). Overall SMPPs could resolve thresholds, but they were often significantly lower than thresholds estimated from in-situ gauging stations and with less discrimination power. Similarly, combining SMPP and soil moisture estimates retrieved from satellite information in California, thresholds for landslide occurrence produced more false alarms than thresholds derived from ground observations (Thomas et al., 2019). Very recently, the spatial pattern of landslides triggered by two storm events in Japan (in 2017 and 2018) was compared to the rainfall pattern retrieved by the IMERG product, the ERA-5 reanalysis, and ground radar observations (Ozturk et al., 2021). In contrast to the radar observations, neither the reanalysis nor the satellite estimates detected a larger rainfall amount in the landslide event area than in the surrounding (stable) hillslopes.

Nevertheless, beyond these few case studies, a global assessment of SMPP to retrieve the properties of rainfall patterns leading to widespread landsliding is still missing. Using ground radar it was recently shown that the rainfall anomaly (i.e., the ratio between event rainfall and past extreme event) better predicts the spatial distribution of landslides caused by a recent typhoon in Japan than the absolute amount of rainfall (Marc et al., 2019). The superior ability of rainfall anomaly as an indicator of landsliding can arise from the co-evolution of the landscape hydro-mechanical properties with the extreme climatology (Marc et al., 2019). Additionally, using anomaly may help to remove bias in mean rainfall retrieval from the SMPPs. Assuming that rainfall anomaly is a valid predictor of landsliding globally, for SMPP to be relevant for landslide hazard alerts, they must retrieve substantial rainfall anomaly, spatially collocated with the zone of landsliding caused by well constrained rainfall events. As the recurrence time of widespread landsliding is relatively rare, large anomalies retrieved by the SMPP should also be rare through time to avoid false alarms.

Here, we focused on 20 storm events for which widespread landsliding has been mapped, to test these two abilities for two high spatial resolution (0.1°), long-standing SMPPs (IMERG and GSMaP) and one hybrid product combining model reanalysis and SMPPs (MSWEP).

2. Data and methods

2.1/ Landslide event inventories

To assess the skills of SMPPs globally, we have tried to gather a large number of landslide inventories spanning a broad range of lithological and climatic setting (Table 1, Figure S1) but other events may have been missed or published after we performed data extraction and analysis (e.g., Coe et al., 2015, Prancevic et al., 2020, Emberson et al., 2022). Most of the rainfall landslide event inventories used in this study (see Table 1) are described in previous compilations by Marc et al., (2018) and by Emberson et al., (2021). In addition, we consider the following landslide event with published inventories: Messina 2009 in Italy (Ardizzone et al., 2012), Hiroshima 2014 in Japan (Wang et al., 2015), and Mocoa 2017 in Colombia (Garcia-Delgado et al., 2019). In all these cases, the boundary of cloud free imagery extends quite beyond the extent of mapped landsliding, suggesting the whole footprint of the landslide event is captured and should reflect a change in rainfall amount (when not limited by availability of steep (>10-15°) hillslopes (Meunier., 2007, Lin et al., 2008, Marc et al., 2019). Additionally, with standard mapping methods (see Stumpf et al., 2014, Marc et al., 2018), we mapped landslides associated with intense rainfall in Japan 2004 (Kondo et al., 2004), Myanmar 2015 (Mondini, 2017) and Haiti 2016 (See Supplementary methods).

Importantly, the landslides themselves usually have dimensions of 10-100 m and their exact locations depend on properties varying at fine spatial scale. Thus, we aim to compare the location and dimension of the area where intense landsliding occurred, spanning from ~50 to >10,000 km² (Table 1), and where rainfall anomaly was retrieved by the rainfall product with a 0.1° resolution (~100 km²). To be sure to detect potentially spatially mislocated anomalies we always extracted rainfall time series over study areas substantially broader than the landslide event area (Table 1).

For Micronesia and Dominica, landsliding was dense across the islands which represents only a few pixels of the rainfall products, and most surrounding pixels being offshore do not allow us to constrain false positives (i.e. strong anomalies without landsliding). As a result, the interpretation and discussion of the spatial pattern of the anomaly relative to the landslides is more limited.

Event Place; Code; rainfall period	[Boundaries °N ; °E]	Landslide Distribution area (km2)	Meteorological data and approximate duration (<10h /10-30h / 30-90h / >90h)	3h/48h max rainfall intensity [I - G - M] (mm/hr)	GLIM Lithology (Köppen-Geiger Climate)	References
Micronesia; MI2; 2002/7/02	[7/7.75 ; 151.25/152.25]	250	I/G/M + g (10-30h)	80/15 - 30/15 -90/33	BA/LF (Af)	Harp et al., 2004, 1
Japan, Kii; J04; 2004/9/28-29	[33/35 ; 134.5/13	200	I/G/M + R (10-30h)	50/10 - 30/5 - 130/14	SM/P/MT (Cfa)	Kondo et al., 2004, Shuin et al.,

	7]					2012
Taiwan; TW8; 2008/7/15-18	[21.5/25.5 ; 120/122]	3000	I/G/M + g (10-30h)	50/11 - 40/13 -200/50	SM/MT (Cfa)	1
Brazil; B08; 2008/11/20-25	[-27.5/-26 ; -50 /-48.25]	1000	I/G/M + g (>90h)	10/2 -7/1.5 - 100/20	MT (Cfa)	Camargo 2015, 1
Taiwan; TW9; 2009/8/6-9	[21.5/25.5 ; 120/122]	11,000	I/G/M + g (30-90h)	100/25 - 30/22 - 150/100	SM/MT (Cfa)	1
Italy; IT9; 2009/10/01	[37.5/38.5 ; 15/15.5]	20	I/G/M + g (<10h)	10/1 - 10/1 - 25/3	MT (Csa)	Ardizzone et al., 2012
Brazil; B11; 2011/1/11-13	[-23/-22 ; -43.5 /-42.5]	1500	I/G/M + g / L (10-30h)	25/4.5 - 25/4.5 - 80/18	PA/MT (Cfa)	1
Japan, Kii, J11, 2011/9/2-5	[33/35 ; 134.5/137]	5,000	I/G/M + R (30-90h)	45/9 - 30/10 - 40/18	SM/P/MT (Cfa)	1
Japan, Hiroshima; J14; 2014/8/20	[33.8-34.7, 132.4-133.4]	30	I/G/M + R (<10h)	27/3 - 23/2 - 50/5	PA/VA/SS (Cfa)	Wang et al., 2015
Colombia; C15; 2015/5/17-18	[5.5/6 ; -76.5/-75.5]	50	I/G/M (<10h)	25/3 - 7/1 - 20/3	MT (Af)	1
Myanmar; M15; 2015/7/15-30	[21/ 24.5 ; 92.5/94.5]	8-10,000	I/G/M (>30h)	15/4 - 15/5 - 80/30	SM/SS/MT (Cwa)	Mondini, 2017
Dominica; D15; 2015/8/27	[15.1-15.7, -	700	I/G/M (10-30h)	55/7 - 40/8 - 150/33	VI (Aw)	UNOSAT 2016

	61.5—61]					
Haïti; H16; 2016/10/1-6	[18/19; -75/-72.5]	400	I/G/M (10-30h)	10/3.5 - 15/5 - 130/55	VB/SM (Aw)	This study
Colombia; C17; 2017/4/1	[0.75/1.5; -77.25/-76.25]	40	I/G/M (<10 h)	10/2 - 8/1.5 - 60/10	SM/SS ()	Garcia-Delgado et al., 2019
Japan, Fukuoka; J17; 2017/7/7	[33/34 ; 130/131.5]	350	I/G/M + g/R (<10h)	30/5 - 25/5 - 30/10	V/PY/MT (Cfa)	Ozturk et al., 2021
Dominica; D17; 2017/9/18-22	[15.1-15.7, -61.561]	700	I/G/M (10-30h)	25/5 - 30/7 - 110/29	VI (Aw)	van Westen and Zhang, 2018
Philippines; P17; 2017/12/20-26	[7-8, 123-125]	40	I/G (10-30h)	25/3 - 20/3 - NA/NA	VA (Af)	2
Japan, Hiroshima; J18; 2018/7/ 5-8	[33.8-34.7, 132.4-133.4]	2500	I/G + g/R (30-90h)	45/8 - 20/5.5 - NA/NA	PA/VA/SS (Cfa)	Ozturk et al., 2021
Philippines; P18; 2018/9/15-20	[16-17 120-121]	50	I/G (10-30h)	40/6 - 30/9 - NA/NA	SM /VA (Am)	2
Zimbabwe; Z19; 2019/3/15-19	[-20/-18; 32/34]	1000	I/G (30-90h)	12/4 - 20/4 - NA/NA	MT/SS (Cwb)	2

Table 1. Data summary for the studied rainfall induced landslide event. I=IMERG, G=GSMaP, M=MSWEP, R=Radar, L=Lightning, g=gauges, NA: Not Available. Abbreviation for litholgical units (see Hartmann and Moosdorf, 2012) and climatic regimes (see Kottek et al., 2006, Figure S1) : BA=Basaltic; LF=Lava Flows; MT=Metamorphic; SS=Siliciclastic; SM=Sedimentary ; P=Plutonic ; V=Volcanic ; A=Equatorial; C= Warm Temperate; f=fully humid; s=summer dry: w=winter dry; m=monsoonal; a=hot summer; b=warm summer. 1 refers to Marc et al., (2018) and 2 to Emberson et al., (2022). Duration is simply given as an order of magnitude to differentiate short events from intermediate, to long ones (Also see Figure S2 for some examples of rainfall event time-series).

2.2/ Satellite Multi-sensor Precipitation Products

In this study we used three satellite-based precipitation products with moderate to high spatio-temporal resolution that are available from 2000 to present: i) the 0.1°/30-min NASA's Integrated Multi-satellite Retrievals for GPM (IMERG, Huffmann et al., 2019), ii) the 0.1°/1-h JAXA's Global Satellite Mapping of Precipitation (GSMaP, Kubota et al., 2020) and iii) the 0.1°/3-h Multi-Source Weighted-Ensemble Precipitation (MSWEP, Beck, 2017), which we describe briefly below.

The IMERG and GSMaP multi-satellite precipitation estimates are based on a combination between the thermal infrared (IR) observations from geostationary satellites and the passive microwave (PMW) observations from all the available satellites from the GPM constellation, either imagers or sounders. Additionally, in-situ observations, from the Global Telecommunication System (GTS) or other gauged-based precipitation product (e.g. CPC, GPCC), are used to readjust (a-posteriori calibration approach) the satellite precipitation estimates. Although IMERG and GSMaP ingest similar raw data, they differ in their retrieval algorithm.

The V06B IMERG algorithm considers the PMW rainfall retrievals from the Goddard Profiling Algorithm version 2017 (GPROF2017, Kummerow et al., 2015; Kidd et al., 2015) and the Precipitation Retrieval and Profiling Scheme version 2019 (PRPS2019, Kidd et al., 2021a). The PMW rainfall retrievals are then combined and inter-calibrated with three prior multi-satellite algorithms, the TRMM Multi-satellite Precipitation Analysis (TMPA, Huffman et al., 2007, 2010), the Climate Prediction Center (CPC) Morphing-Kalman Filter Lagrangian time interpolation scheme (CMORPH-KF, Joyce et al., 2004, Joyce and Xie, 2011) and the Precipitation Estimation from Remotely Sensed Information using Artificial Neural

Networks-Cloud Classification System re-calibration scheme (PERSIANN-CCS, Hong et al., 2004). Moreover, V06B incorporates several other major improvements to the algorithm, including, for instance, a homogenous GPM-TRMM calibration, a new model-based morphing scheme and refinements of the Kalman filtering and the quality index. IMERG precipitation estimates are available twice in near-real time (the Early and Late runs), which the calibration consists in climatological gauge adjustments (using GPCP), and a post-real-time (Final run - Multi-satellite precipitation estimate with gauge calibration) which considers monthly gauge analyses for the adjustments.

The V6 GSMaP algorithm utilizes distinct approaches for retrieving the precipitation over land and ocean surfaces, and when orographic rainfall is expected. The retrieval is performed differently depending on the radiometer type through the successive application of three algorithms: the Microwave Imager/Sounder Algorithm (GSMaP_MWIS, Kubota et al. 2007; Aonashi et al. 2009), for calculating the rainfall rate from PMW platforms; the MW-IR Merged Algorithm (GSMaP_MVK, Ushio et al., 2009) using the Morphing Kalman filtering approach to better constrain the affected areas and their rainfall rate; and the Gauge-calibrated rainfall algorithm (GSMaP_Gauge, Mega et al., 2019), by adjusting the GSMaP_MVK estimates with the NOAA's global gauge analysis (CPC Unified Gauge-Based Analysis of Global Daily Precipitation). The GSMaP rainfall estimates are available at three levels, namely, real-time, near-real-time, and standard products (GSMaP_MVK and GSMaP_Gauge).

In contrast to IMERG and GSMaP, the MSWEP V2 precipitation estimates are the result of a combination between the gridded precipitation data from satellite estimates, climate models reanalyses and various global gauge networks (see the list of products in Beck et al., 2017). The methodology underlying MSWEP involves multiple and sequential approaches to take advantage of all those distinct products to compute the optimal merging of precipitation estimates. In general, it considers distribution and systematic bias corrections, globally and regionally by utilizing daily precipitation observations. Note that MSWEP is not strictly speaking a SMPP as it blends satellite measurements with model reanalyses and rain gauge measurements. Thus, its inclusion is aims to assessing the pros and cons of GSMaP and IMERG, which have the potential to produce nowcast and hazard alerts for heavy rainfall and landsliding in the coming years (Otsuka et al., 2016, Kotsuki et al., 2019).

Therefore, in our investigation, we have extracted rainfall estimate time-series from IMERG Final Calibrated V06B, GSMaP Gauge V6 and MSWEP V2 , in regions surrounding each considered landslide event (Table 1). This covers the period from mid-2000 to the end of 2019 for GSMaP and IMERG, but for MSWEP we could only access data until 11/2017 preventing us from studying the four most recent events with this product (Table 1). Given the variable start date of each product, we also discarded the record of each product before 01/01/2001.

2.3/ Estimation of rainfall anomaly from SMPP

To assess the relevance of the satellite rainfall products to understand landslide events we propose to use the rainfall anomaly metrics of Marc et al., (2019). The authors found that the spatial distribution of landslides caused by a large typhoon mismatched with the spatial pattern of total rainfall during the typhoon, Rt, but agreed with the one of rainfall anomaly, R*, defined as:

$$R^* = Rt / R10 \qquad \text{(Eq. 1)}$$

with R10 being the 10-year return rainfall. The anomaly is defined at each gridcell and over any timescale relevant to landsliding; e.g. 3h, 12h, 48h and 96h for which both Rt and R10 are computed in this study (Figure 1). As it is based on a ratio, the anomaly metric may also remove potential bias of underestimation or overestimation of rainfall in some areas, as long as within a single pixel this bias is systematic through time and thus affects both Rt and R10. Still, some bias is likely to remain as the accuracy of SMPPs' retrieval (especially in rugged terrain or during heavy storms) varies through time, both over yearly and decadal timescales because the satellite constellation has changed, and at the event scale, depending on radar overpasses.

To compute the rainfall anomaly, we first computed R10 for all study areas using the Metastatistical Extreme Value distribution (MEV, Zorzetto et al., 2015). We calculated a time series of mean rainfall rates at a given timescale, excluding every timestep where the mean rain rate was below 0.02 mm/hr (~0.5mm/day typically in the range of thresholds used to consider dry days (0.1-1mm/day); Reiser and Kutiel, 2009) and applied the Probability Weighted Moment method to fit a Weibull (a stretched exponential) distribution to the remaining data of each annual block. Then we derived the MEV cumulative distribution function, as an average of the sample constituted by all the annual Weibull distributions, from which we extracted the 10-year return rainfall. This method using the whole rainfall dataset is expected to be more robust than fitting a General Extreme Value (GEV) distribution on the annual maxima (Zorzetto et al., 2015, Marra et al., 2018, 2020). For reference, we have also computed R10 through a Maximum Likelihood fit of a GEV distribution to the empirical distribution of annual maxima (Saito and Matsuyama, 2012, Marc et al., 2019). This approach yielded R10 maps with similar spatial pattern but with increased magnitude over some zones, typically by 20 to 100 %.Thus, this approach would decrease somewhat the reported anomalies but not change their locations nor our conclusions.

Having mapped R10 over the areas of interest, we compute the maximum total rainfall that occurred over the considered timescales (3h-96h) within a period of 5-15 days containing the storm-induced landsliding event (see Table 1, Figure 1), as well as within each annual block of the time series. Thus we estimate the rainfall anomaly both during the event, and for every year of record, allowing to assess both whether a given product retrieved or not a strong anomaly associated with large landslide events, but also whether they have recorded large anomalies during other time periods, which may be other landslide events or false alarms (Figure 2). Note that, if the maximum rainfall rate of the annual block in which the event occurred, is outside of the event time window, then the event and annual anomaly will be different.

The four timescales over which both the event and annual anomalies were computed should allow capturing both landslide events driven by short intense bursts of rainfall and by more prolonged rainfall (see Table 1, Figure S1). We did not use timescales shorter than 3h as it would exclude the MSWEP product and as the reliability of such short-term measurement on small areas is debated (Guilloteau et al., 2016).

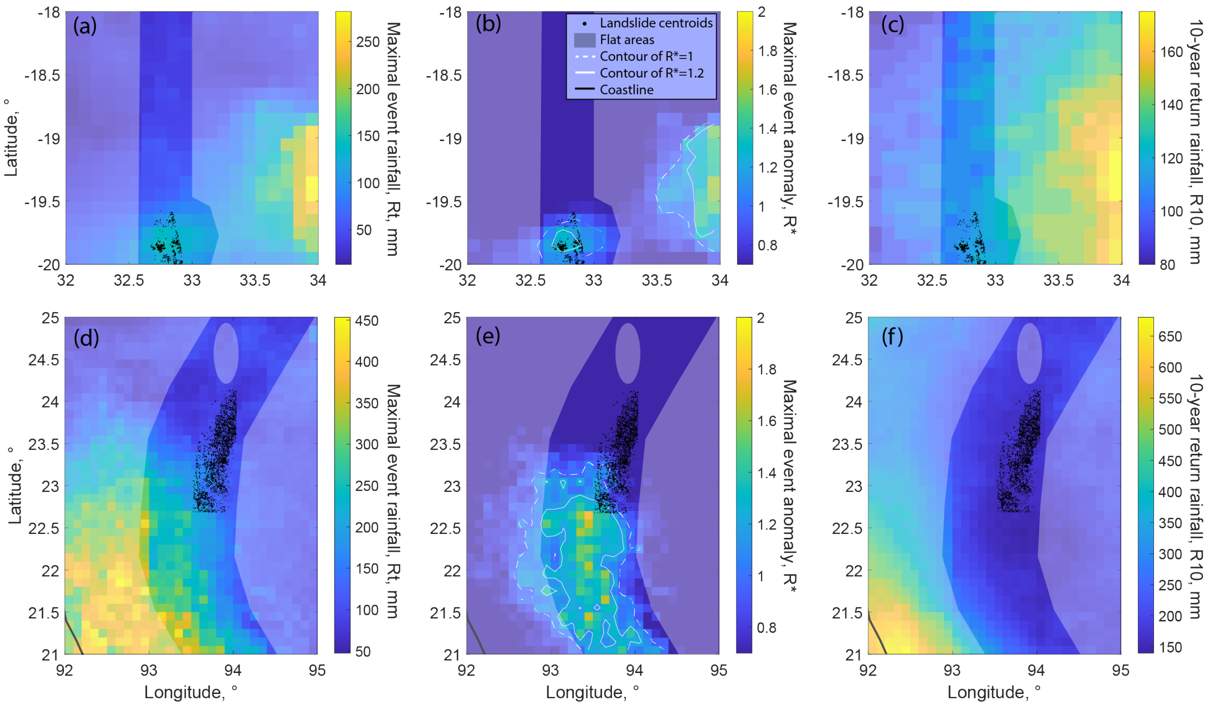

Figure 1: Total rainfall (Rt, mm), rainfall anomaly (R*=Rt/R10) and 10-year return rainfall (R10, mm) obtained from GSMaP at 12h timescale during Z19 (a-c) and from IMERG at the 48h timescale during M15 (d-f). Black dots are landslide centroids, shaded areas are relatively flat terrain where landsliding is unlikely, and white solid and dashed lines (b, e) are anomaly contour for R*=1.2 and R*=1, respectively.

2.4/ Categorizing the skills of the SMPP for each event

For each landslide event, we aim to categorize the spatial and temporal skills of indicators derived from the SMPPs. Given that the link between landslides and rainfall is not straightforward, fully parameterized extraction and comparison of "rainfall objects" (see Davis et al., 2006) defined based on R* and landslide density may artificially degrade this link or require too many parameters to be adjusted. Issues would be similar with approaches based on spatial averaging (see Robert and Lean, 2007). However, our objective is not (yet) to develop a specific method to routinely compare landslides and retrieved rainfall, but only to understand in which settings SMPPs retrieve spatial rainfall patterns consistent with the associated landsliding, if at all. By focusing on a few specific cases, one could follow the approach of Ozturk et al. (2021), comparing an empirical model based on static layer only (e.g., slope, geology) to one based on the same static layers complemented with a rainfall map. However, given the number of studied events (20), the number of rainfall anomaly timescales (3) and the number or years evaluated for the temporal skill (>15) such an approach would have been impractical and excessive regarding our goals. Thus, as a preliminary approach for our dataset, we manually inspected each event and evaluated the qualitative agreement of the retrieved anomaly and landslide pattern, through space and time.

To assess the spatial skill of the rainfall product qualitatively, we focus on the overlap between significant rainfall anomalies (i.e., R*>1) and the area of intense landsliding (i.e., ignoring isolated landslides) (Figure 1). When the overlapping area is similar or larger than the mutually exclusive areas (excluding flat and submerged area with R*>1), the spatial skill is deemed good (Fig 1b, 2e, 5d-f, 7). If the rainfall anomaly contains the landslide area but extends much beyond, it is ranked as fair (Fig 2a, b, f). If the rainfall anomaly is offset from the landsliding area but within a range smaller or similar to the dimensions of the landslide event (taken as the small axis of an ellipse containing most of the landslide) it is also deemed fair (Fig 1e). Finally, when the rainfall anomaly is further away but still in the study area it is considered poor (Fig 2i, j).

The temporal skill is based on the intensity of the anomaly within the boundary of the landslide event during the event relative to other annual maxima, as in most areas we have no other substantial landslide events reported over the period (Figure 2). If the rainfall anomaly was the largest during the last 20 years, we consider the temporal skill is the best possible, and false alarms are unlikely. If the rainfall anomaly was ranked 2nd or 3rd, the skill is fair as false alarms are possible but rare, while if the anomaly has a lower rank the skill is poor and false alarms are likely (Figure 3). Note that for J04, D17 and TW8, given the affected areas overlap with the larger storms and landslide events which occurred in 2011, 2015 and 2009, respectively (see Table 1), the temporal skill is best when the anomaly is ranked second behind these events. In the discussion, we will also address the possibility that some other strong anomaly retrieved by the SMPP could correspond to other landslide events reported in the literature (especially in Taiwan and Japan) or to landslide events unreported.

When the anomaly at all timescales remain weak (R*<1) during the event, it is considered undetected by the rainfall product and both skills are null. Given that landslides can be triggered by either short or long rainfall, we record for each event the timescales yielding the best spatial and temporal skill (Supplementary Figures S2 to S12), and will focus on these timescales in the following results and discussion.

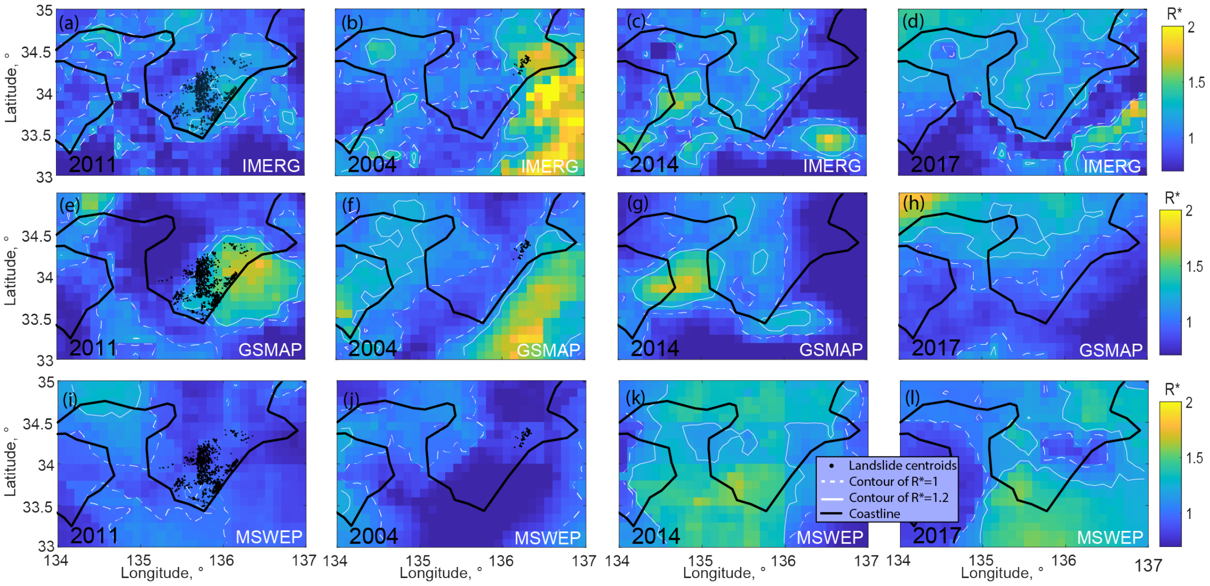

Figure 2: Maps of the maximal annual anomalies at 48h, for 4 selected years over the Kii Peninsula (Japan), for IMERG (a-d), GSMaP (e-h) and MSWEP (i-l). Black dots show landslide centroids from two major landslide events that occurred during Typhoon Meari and Talas in 2004 (b,f,j) and 2011 (a,e,i), respectively. The timing of these maxima is in Figure S13.In spite of large anomalies, no landslide events were reported in 2014 and 2017.

3/ Results

In most cases, at least two products have detected substantial anomaly (R*>1) over at least one timescale during the events triggering landsliding (Figure 3). However, beyond this basic "regional" detection, we note that the rainfall products often have fairly diverse spatial and temporal skills, even though they used the same satellite constellation as a primary source of data. Below, we briefly detail this diversity of performance by reviewing each case. Note that except for MSWEP for J11, the 96h timescales is systematically less or similarly skilled to shorter timescales (Figure 4), and thus it won't be described in details.

3.1/ Case by case anomaly patterns and skills

For some events all products retrieved similar anomaly patterns, such as MI2, and D15 where all products retrieved R*>1.5-2 all over the island (and often the ocean) at 48h and 12h respectively. Similarly, for B11 at 12-48h and TW9 at 48h, all products retrieved anomaly in or near the landsliding area R*~1.4 and R*~1.5-2 respectively. For these four cases the event anomalies were the largest in the area for 20 years. For M15, all products also retrieved R*~1.2-1.4 at 48h, on the southern edge of the landslide area (Figure 1) but the temporal skill varied, as the event anomaly was ranked 1st, 3rd and beyond 6th for MSWEP, GSMaP and IMERG, respectively. For J04, all products retrieved an anomaly (R*~1-1.5) over the landslide area and ranked it as the largest in the northeastern part of the Kii peninsula for the last 20 years. However MSWEP and IMERG had the anomaly spreading over a much larger area than the one experiencing landsliding, and the timescales with the strongest anomaly varied from 3 to 48h for the three products (Figure 3). For P18, both GSMaP and IMERG retrieved R*~1.2 at 12h on the eastern edge of the landslide zone, but none retrieved this anomaly as the strongest of the timeseries. Similarly, for J18 both GSMaP and IMERG retrieved R*~1.2-1.4 at 48h and 12h respectively, on the eastern edge of the landslide zone but found a stronger anomaly to have occurred in October 2017.

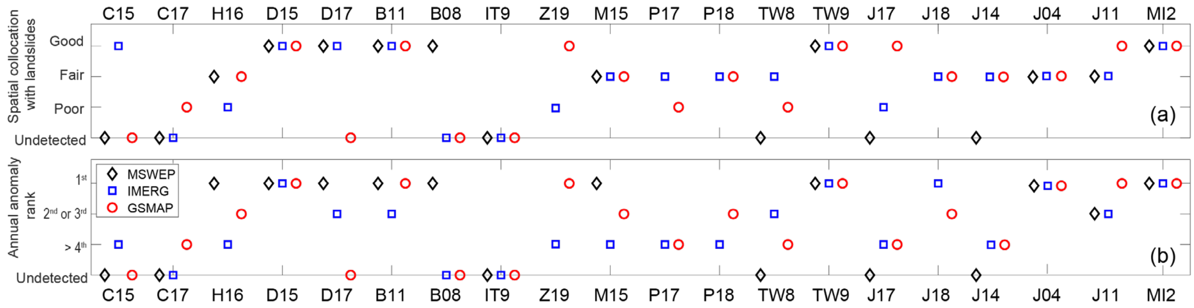

Figure 3: Spatial (a) and temporal (b) skills of the three rainfall productsfor the 20 rainfall-induced landslide events.

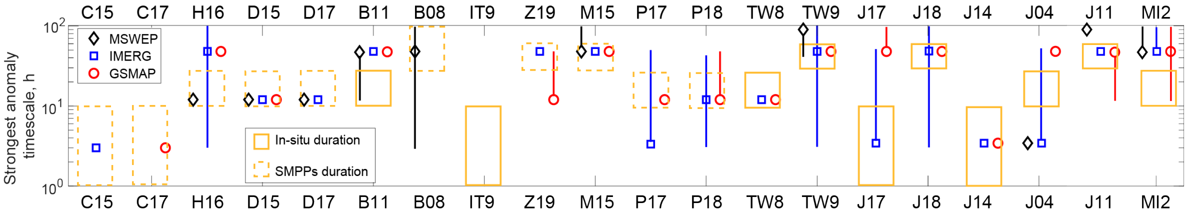

Figure 4:Timescales at which occurred the strongest anomaly for the 20 landslide events and the three rainfall products. Vertical bars indicate similar spatial and temporal performance were obtained at several timescales.

Other landslide events are not retrieved in terms of rainfall anomalies. For H16, MSWEP retrieved R*>1.4 over the whole peninsula at 12-48h, GSMaP found a modest R*~1-1.2 at 48h, localized at the peninsula's tip and IMERG found a very small and weak (R*~0.9-1) anomaly 10-20 km east of the landslide event area. For J11 at 48h, GSMaP and IMERG found R*~1 and R*>1-1.4 in the landslide event area, and ranked 1st and 3rd annual anomaly of the time series, respectively. MSWEP yield similar results but only at 96h. J14 was not detected by MSWEP, but both GSMaP and IMERG found a weak anomaly (R*~1) at the 3h timescales, next to the landslide area but with many false alarms (larger anomalies) recorded for other years. We note that the anomaly is a bit stronger at 2h which makes sense given the intense rainfall was just limited to 2h (Wang et al 2015). For J17, MSWEP did not detect any anomaly, and GSMaP and IMERG detected a small R*~1-1.2 overlapping with or 10 km eastward, respectively, of the landslide event. For TW8, MSWEP did not retrieve significant anomaly, while IMERG found R*~1-1.2 at 12h mostly collocating with the landslide clusters, and GSMaP found an anomaly of R*~1.2 located mostly on the flat coast west of the landsliding. For P17, MSWEP was not available and both SMPPs retrieved some pixels with R*~1-1.2 near the landslide events, but they all had many other years with similar annual anomalies. For Z19, both SMPPs found R*>1.5 at 12-48h more than 100 km East of the landslide event, over flat areas, and only GSMaP found R*~1.4 precisely collocated, in space and time, with the landslide event.

Last, some events were retrieved by only one product, such as B08 where MSWEP only found a localized R*>1, at all timescales, C15 where only IMERG detected R*>1 locally , and C17 where only GSMaP found R*~1-1.2, but about 100 km Northeast of the landslide event. Finally, IT9 was simply undetected by the three products.

3.2/ Global performance and relation to timescales

For the studied events, the three products have similar performance spatially and temporally, with only a third of good retrieval, and with some false alarms and poor to fair localization in most cases. For each product, the spatial and temporal skills are quite strongly correlated, though IMERG is more often better for spatial accuracy, while GSMaP is more often better for temporal accuracy (Figure 3, S14). Given our limited landslide inventory sample, we do not attempt to evaluate if skills are varying by geographical regions. However, we note that the skills of the products do not seem related to the year of the event, with some poorly retrieved events occurring both in the TRMM era (B08, IT9, TW8) and the GPM era (C15, C17, P17).

In spite of the variable ability to retrieve a spatial anomaly collocated with landsliding or to rank the annual events from 2001 to 2019, the three products agree most of the time in terms of the timescale over which the maximal rainfall anomaly occurred during the landslide event (Figure 4). Indeed, in most of the Asian and Pacific typhoons cases (TW9, J11, J18, M15), the products display the strongest anomaly with the best spatial match at the 48h hour timescale. This appears to be the good order of magnitude for the intense rainfall duration between 1 and 3 days (Table 1). For TW8, D15, D17, and P18 all products suggest the anomaly best related to the landsliding was at the 12h timescale, which can only be confirmed from in-situ data for TW8. Though more uncertain and retrieved only by some products, C15, C17 and J14 only have anomalies at 3h timescales consistent with the ideas that they were short, localized intense rainfall (Wang et al., 2015).

Still for 6 other cases (MI2, H16, P17, J04, J17, Z19), the timescales of different products disagree and do not necessarily match the duration of absolute rainfall records.

4/ Discussion

4.1/ On the importance of normalizing absolute rainfall estimates

We note that although the three products often had rainfall anomalies which shared similarity in terms of spatial and temporal patterns, they would have been much more difficult to compare with absolute values. Indeed in terms of absolute rainfall the location and amount retrieved by the three SMPPs could easily vary by more than a factor of 2, making any quantitative comparisons between the products and empirical or physical thresholds very difficult.

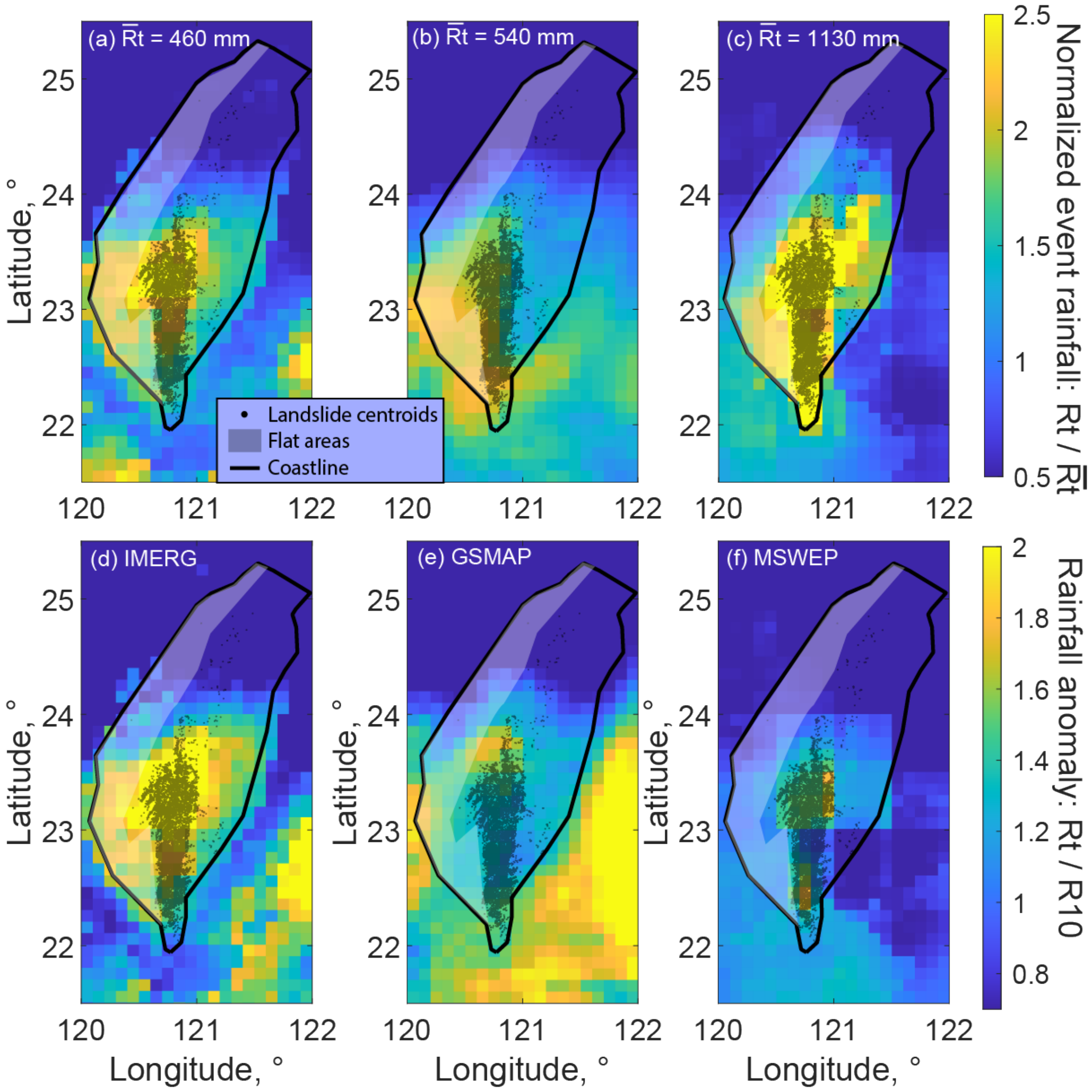

Figure 5: Maps of total event rainfall normalized by the mean event rainfall over the study area (a-c) and rainfall anomaly (d-f) at 48h during Typhoon Morakot for the three rainfall products. Centroids of landslides triggered by Morakot are in black, and flat coastal areas not prone to landsliding are within the shaded area. Note the diversity of patterns and magnitude of absolute rainfall among rainfall product and how it is reduced when computing rainfall anomaly.

For example, during Typhoon Morakot (TW9) and Meari (J04), the total rainfall during 48h over the area with widespread landsliding was about 800 mm and 500 mm for IMERG, 1200 mm and 250 mm for GSMaP and 4000 and 700 mm for MSWEP respectively (Figure 5, S6). For the area with landsliding in M15 and J11, the 48h total rainfall was about 300 and 400 mm, respectively, for both IMERG and GSMaP, while in the same area MSWEP reported about 1500 mm and 800 mm, respectively. Independent gauge or radar estimates available for TW9, J04 and J11 suggest 48h rainfall amounted to about 2000 mm, 800 mm and 1000 mm (Kondo et al., 2004, Chien and Kuo, 2011, Marc et al., 2019), suggesting none of the SMPP were correct and that it would be very difficult to build and compare threshold in terms of absolute rainfall. Similar bias and variability can be found at short timescales, for example, in 3h during J14 event, in the landsliding area, GSMaP and IMERG recorded about 75 mm in 3h while MSWEP recorded 150 mm. All products underestimated the event rainfall measured by radar to 220 mm in 3h (Wang et al., 2015), but interestingly though MSWEP was the closest in absolute term it is the only product which did not yield any anomaly, given its R10 of 250 mm in this area (Figure S7). These large differences in absolute rainfall at short- and long- timescales likely come from the fact that different gauges are used for normalization, and that GSMaP uses an orographic rainfall boost under some conditions, while MSWEP may, in some cases, revert to the reanalysis modeled rainfall rather than the satellite measurements. For the 20 storm events, the diversity of mean rain rates leading to landsliding (whether at short- or long- timescales) is also very large from about 5 mm/hr to >100 mm/hr, which underlines the difficulty in looking for global threshold in absolute rainfall intensity.

Beyond intercomparison and comparison with thresholds, the effect of a normalization by R10 also allows to account for strong gradients in the extreme climatology that could be misleading when trying to anticipate the location of landslide hazard. For example, M15 and Z19 both have much stronger Rt towards the coast, in relatively flat areas, and it is when computing R* that it becomes clear that the mountainous areas had actually exceptional rainfall with R*>1.2 on or near the landslide event area (Figure 1).

4.2/ Are other extreme anomalies false alerts or unreported landslide events? Insights from Taiwan and Japan.

Among the studied areas, only some parts of Taiwan have been mapped systematically to identify landsliding caused by multiple typhoons within the same areas. Marc et al., (2015) mapped the landslides caused by rainfall events between 1996 and 2014 within the Chenyoulan catchment in central Taiwan (23.5-24°N). Huang and Montgomery reported intense landslides in 2001, 2004 and 2005 along the Tachia river (about 24°N), while Chen et al., (2013) mapped the impact of more than 10 Typhoons in three catchments across Taiwan (Figure 6). Given not all of these studies report landslide area density, at first order we use landslide number density as a measure of the relative magnitude of the landslide event caused by various typhoons. In the Northern catchment (24.5°N), they could constrain only the typhoons between 2004 and 2009, and found that intense landsliding (>1 per km^2) occurred in August 2004 and 2005, during typhoons Aere and Matsa, respectively. In the two southern catchments (23°N) they reported most landslides during Morakot (TW9, >1 km^2), then during typhoon Haitang in July 2005 (~0.5 km^2). Three other typhoons induced similar landsliding (0.1-0.2 km$^{2)}$, typhoons Mindulle, Bilis and Kalmaegi (Here TW8), in early July 2004, 2006 and 2008, respectively, while other events caused significantly fewer landslides.

In Taiwan, the pattern and timing of the maximum annual anomalies is quite similar for the three SMPPs, and the following discussion applies to all SMPPs. In 2001, a very strong anomaly hit northern Taiwan (25°N) in September 2001 corresponding to typhoon Nari, while a more modest anomaly in late July near 24°N corresponding to typhoon Toraji which caused widespread landsliding between 23.5 and 24°N(Huang and Montgomery, 2013, Marc et al., 2015). Substantial anomalies are also present from 24°N to 22°N in July 2005 and near 24°N in July 2006, matching well with typhoons Haitang and Bilis, although the anomalies are not stronger in 2005 as could be expected from the landsliding and the gauge measurements (Chen et al., 2013, 2015). Surprisingly the typhoons which have caused landsliding in the North in 2004 and 2005 (Aere and Matsa) have not been recorded with strong anomalies (Figure 6b, 6g). However, from 24.5 to 25.5° moderate but extensive anomalies were retrieved in October 2007 and September 2008, matching with typhoons Krosa and Sinlaku which caused some landslides in northern Taiwan (Chen et al., 2013). However, these two years the typhoons causing landslides in the south (Sepat in 2007 and Kalmaegi in 2008) were not retrieved consistently with the poor spatial and temporal score achieved for TW8 (Fig. 3). So it seems clear in the case of Taiwan, that across the last decades many of the strong anomalies were indeed strong typhoon events which did cause landsliding (Figure 6), and the poor score of TW8 seems rather due to some misdetection of this event rather than false alarms for other typhoons. Nevertheless, the rainfall anomaly in 2012 appears as a false alarm, and several rainfall-induced landslide events are associated with R*<1 or mislocated anomalies (Figure 6).

Figure 6: Eight strongest maps of annual maxima of 48h rainfall anomalies from IMERG over Taiwan. Landslides centroids from TW8 and TW9 are shown as black dots (a, f). Major landslide events reported

from the literature (see text) are in solid red (intense landsliding, >0.5 km^{-2}) or dashed red (moderate landsliding, 0.1-0.5 km^{-2}). Results are similar for MSWEP and GSMaP. The timing of these maxima is in Figure S15.

Japan is also a country very prone to landslides and landslide events are often reported in news or scientific reports. Below, we discuss strong anomalies and landslide reports from the literature in the three areas we have analyzed.

In the Kii peninsula, the inter-product variability is higher than in Taiwan but we note that GSMaP, and to some extent MSWEP, retrieve substantial anomaly (R*~1-2) on the Southern and Eastern part of Shikoku island (134°E) in August 2004 (Figure 2). This corresponds to the heavy rainfall caused by Typhoon Namtheum which led to several large landslides in Shikoku island (Wang et al., 2005). In contrast, all SMPPs detect significant anomalies (R*>1.5) on the eastern edge of Shikoku in 2014 and across the peninsula in 2017, while we did not find any reports of landslides for those two years.

Over Kyushu, both SMPPs yield several annual anomalies equal or larger than in 2017, while we could not find mention of other landslide disasters in the area, in the literature or the international disaster database EM-DAT. Over Hiroshima, J18 is clearly among the largest anomalies, but October 2017 also appears as the first and second largest anomaly for GSMaP and IMERG respectively. It corresponds to typhoon Lan which has caused flooding and some landsliding over several prefectures of Honshu island (EM-DAT). Additionally, even if J14 yields R*~1 at short timescales, well collocated with landsliding, many years have stronger anomalies without reported landsliding, suggesting some underestimation.

In summary, in Taiwan, most annual maxima of rainfall anomaly correspond to major typhoons which have caused landslides and the problem is rather that some events are underestimated. In Japan, it is less clear, and while some major anomalies correspond to other landslide or flooding events (Shikoku, 2004, Hiroshima 2017), we also find that several annual anomalies may be overestimated. Such false alerts and overestimation of the anomaly may be due to an underestimation of R10 in some place rather than to the overestimation of the event rainfall. We also note the likelihood of false alarms derived from anomaly ranking is a very rough measure, which has multiple limitations. First, because the techniques were not evaluated globally on landslide prone terrain, but also because we focus on a threshold of R*>1 while this threshold likely varies, for example with lithological units (Marc et al., 2019). This highlights the need for future studies to better understand the source of uncertainties of R10 for each product, as well as to replicate the methods in other geographical areas and with other, landscape adjusted, R* threshold.

4.3 Limits and potential for improvement of the SMPP

In this work we assess the relevance of SMPP to landslide analyses with the working assumption that landslide events are bound to occur on any hillslopes experiencing rainfall amounts (over timescales from 3h to 96h) exceeding the local 10-year return rainfall, as shown for J11 (Marc et al., 2019). The use of the ratio of event rainfall to R10 is consistent with the geomorphological concept (Dietrich et al., 1995, Iida, 2004, Marc et al., 2019) that the stability of the landscape is adjusted to the climate and in particular the extreme meteorology.

All events except B08 being shorter than 100h, it is unlikely that poor performance in some cases could be resolved by an analysis over longer timescales. However, the focus on rainfall anomalies ignores the fact that landslides are caused by a rise of pore water pressure that may only partially relate to the ongoing rainfall, and be in large part due to antecedent rainfall and hydrological processes modulating the subsurface drainage (Bogaard and Greco, 2018) and the water storage in the slope aquifer (Bronimann et al., 2013; Watakabe and Matsushi, 2019), all of these processes being modulated by the slope fabrics and fracturing. As a result, a future approach could aim to couple a simple model to estimate the water level in the regolith based on the rainfall time-series (e.g., Wilson and Wieczorek, 1995) and focus on anomalies of regolith water level (e.g., Saito and Matsuyama 2012). Combining rainfall products with satellite-based soil moisture estimates could also be a way forward (Felsberg et al., 2021). Still, in the cases of sustained heavy rainfall, characteristic of many events of this study caused by typhoons and hurricanes, the moisture from antecedent rainfall is likely negligible relative to the one brought by the event. Beyond antecedent rainfall, the rainfall regime as well as hydromechanical properties of the ground modulate landslide triggering, likely affecting the ability of SMPPs to retrieve the conditions of landsliding. Though our global analysis covers many typical landslide settings (Table 1), it is not sampling them equally, especially in terms of climate (temperate and equatorial fully humid settings, represent more than half our database). Additionally some specific settings are not represented such as landscape with carbonates topography, or with “arid”, “snow” or “polar” climates less common but present in areas prone to landsliding such as the Alps, Norway, Central Asia and the edges of the Tibetan Plateau (Figure S1). Future studies should aim at constraining these undersampled settings as well as assess the skills of SMPPs in specific settings which may be associated with peculiar landslide triggering (e.g., orography, atmospheric rivers, rain-on-snow events, monsoons and very long duration (week) precipitation events).

4.3.1 SELECTED EVIDENCE ON INCORRECT RAINFALL RETRIEVAL

For a number of rainfall induced landslide events, we lack independent rainfall in-situ measurements. Thus the discrepancy between satellite anomaly maps and landslide locations may not necessarily be due to a mis-retrieval of the rainfall by the SMPP, but could also be due to some additional variability in factors controlling the landslide location, such as the strength, permeability and infiltration rate, slope gradient and vegetation state of hillslopes. However, in a number of cases, in-situ rainfall data reported intense rainfall activity collocated with the landsliding which suggests that the SMPP rainfall retrieval is in large part at fault. This was clearly the case for J11 where the rainfall anomaly estimated from radar observations agreed precisely with the area of landsliding (Marc et al., 2019). The same was true when considering total event rainfall for J17 and J18 (Ozturk et al., 2021). This was also likely the case for TW9 and IT9 which all had exceptional levels of absolute rainfall in the area where most landslides occurred (Chien and Kuo, 2011, Ardizzone et al., 2012). On these four events, only TW9 was well retrieved by all products, though even in this case the quantitative pattern of R* at fine scale is quite different in each case (Figure 3). The retrieval for the Japanese case was quite variable and IT9 was completely undetected by the three products.

The two Brazilian landslide events also highlight the issue with the current retrieval of SMPP. B08 was completely undetected by GSMaP and IMERG, and the detection by MSWEP may be entirely due to a local gauge nearby (Camargo et al., 2015) which recorded heavy rainfall on the two days preceding the events, at the end of an anomalously wet month.

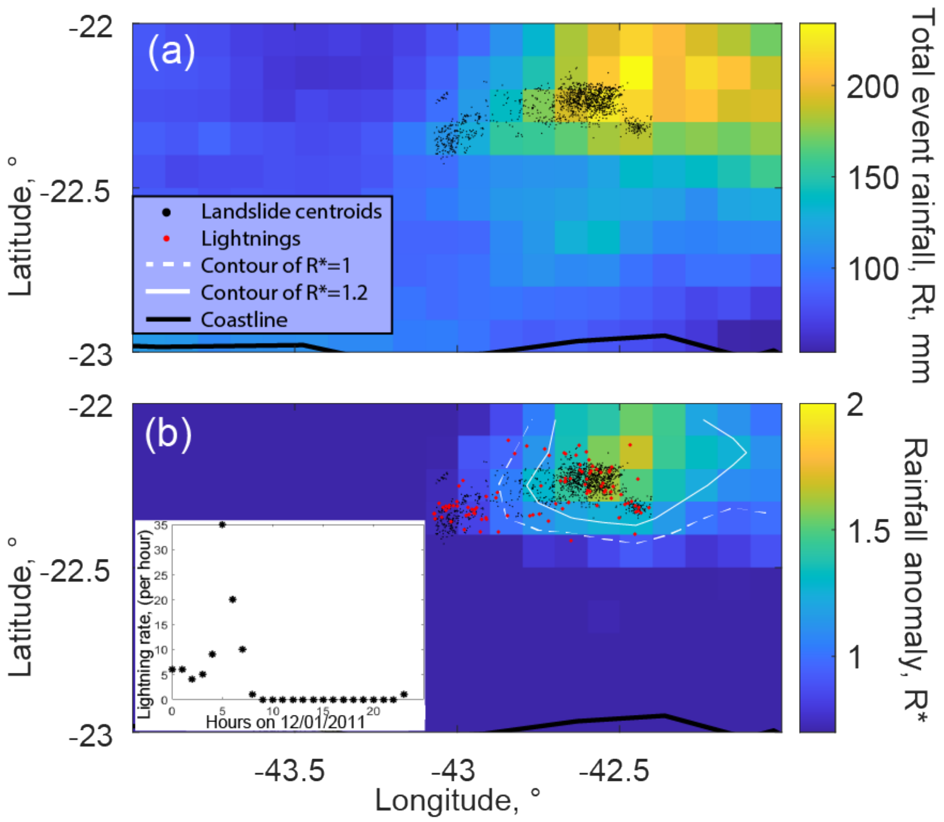

Figure 7: Event rainfall (a) and anomaly (b) at 48h timescale for GSMaP in January 2011 in Brazil. Black dots are landslide centroids and white solid and dashed lines (b) are anomaly contour for R*=1.2 and R*=1, respectively. Results are almost identical for IMERG and MSWEP. Recorded lightning locations on the 12th of January are shown by red dots in (b) and their timing is in the inset. In comparison, lightning activity on the 11th and 13th was much weaker.

For B11, the three SMPP broadly agreed during the event and retrieved a strong anomaly between 12 and 48h, overlapping with most of the landsliding slightly offset to the northwest of the landsliding area (Figure 6). For this event, the Brazilian lightning record show intense lightning activity precisely collocated with the three clusters of landsliding (Figure 6). The link with the landslides is even more striking considering that most of the lightning of this day occurred between 5 and 7 AM local time, which matches well with the timing of several destructive landslides in urban areas reported between 6AM and 9AM on the 12th of January (Netto et al., 2011).

Strong lightning activity at the time of landsliding was reported for older disasters in Brazil (Jones, 1973), even leading to the suggestion that they may directly induce landsliding (Lacerda, 1997). However, it is well known that lightning activity is associated with intense convection and intense bursts of rainfall (Battan, 1965; Piepgrass et al., 1982; Soula and Chauzy, 2001; Schulz et al., 2011), which strongly suggests that exceptional rainfall intensity must have occurred on the morning of the 12th January, exactly when the landslide occurred, from 42.5 to 43°W. In contrast the three SMPP suggested a strong fading of both Rt and R* from 42.5°W to 43°W (Figure 1).

Thus we propose that, in many of the studied cases, the poor link between SMPP retrieval and landslide location is likely due to inadequate rainfall retrieval from the SMPP rather than due to some independent complexities in the landscape and/or the landslide mapping. In the next section we briefly identify options to improve the SMPP algorithms.

4.3.2 IMPROVING SMPP RETRIEVAL FOR LANDSLIDE APPLICATIONS: INCLUDING LIGHTNING AND OROGRAPHY

As we have seen in the case of B11, the spatio-temporal pattern of lightning seems to accurately match the location of landsliding. Thus, with the recent launch of the Geostationary Operational Environmental Satellite (GOES) satellite, with sensors permitting mapping of lightning activity (Geostationary Lightning Mapper, GLM) with high spatio-temporal accuracy (Goodman et al., 2013), incorporating lightning activity in SMPPs is potentially a way forward for better mapping of extreme rainfall and landslide applications. Physical models to derive quantitative precipitation estimates from lightning activity exist (Minjarez-Sosa and Waissman, 2020) and could be used in conjunction with other highly resolved, continuous measurements (such as the geostationary infrared in PERSIANN; Xu et al., 2013; Mahrooghy et al., 2013). This may prove especially useful in capturing brief and localized events that may form and dissipate without being sampled by the passive microwave radiometers, thus likely strongly biasing their retrieval (Guilloteau et al., 2017). In fact, SMPPs tend to smooth rainrate over scales smaller than 200 km and 4 h, biasing both the intensity, location and timing of precipitation features (Guilloteau et al., 2021).   More generally, uncertainties in SMPPs rain retrieval is highly space-time dependent, as it depends both on environmental conditions (e.g., the precipitation regime, type of precipitation system, surface type), and the technique itself, which involves the combination of distinct uncertainty sources (i.e., the calibration, the algorithm and the sampling terms, Roca et al., 2010). Particularly, among these factors, PMW observations, which are the essential component of IMERG and GSMaP, , are commonly processed through Bayesian-like algorithm(Aonashi et al., 2009, Kummerow et al., 2015), implying certain limitations, for instance in dealing with the platform-sensor heterogeneity and the rainrate variability. Consequently, both the intensity and detection of light and intense rainfall may be biased (Elsaesser and Kummerow 2015; Kidd et al., 2018; You et al., 2021), which also propagates up to the final Level-3 precipitation retrieval (Ayat et al., 2021; Oliveira et al., 2016).

Another issue that may bias SMPP, especially in the case of landslide studies, is the retrieval of orographically forced rainfall. Studies focused on Japan, Taiwan and India, have shown that the radar profile with altitude was strongly affected in the case of upward orographic forcing of warm and humid air masses (Shige et al., 2012; Taniguchi et al., 2013; Yamamoto et al., 2017). As a result, the GSMaP algorithm was updated to differentiate for such orographic conditions, based on reanalyzed wind model and topography. However, the issues in overestimating or underestimating the orographic effect depending on the wind speed has been highlighted for GSMaP v6, and should be corrected in v7 (Yamamoto et al., 2017). Unfortunately, GSMaP v7 has not been reprocessed before 2014 yet and our result based on v6 thus suffers from this inaccurate orographic algorithm. This issue also strongly impacts the maps of R10 (FigureS5c, S8c), leading in the case of TW9 and TW8 to a strong reduction of the anomaly relative to the other SMPP (Figure 4, S6). In the case of J11 this issue is less pronounced and in spite of it GSMaP retrieves a much stronger anomaly (the strongest on record) although a bit offset from the main relief (Figure 2). In any case investigating and updating the orographic algorithm to prevent this bias in rainfall location seems urgent to maximize GSMaP relevance for landslide study. Further developing orographic correction, to also account for other forms of orography than the uplift of warm and humid air masses is also of importance (see review by Houze, 2012).

Lastly, efforts to improve high-resolution SMPPs are constantly ongoing (see Kidd et al. (2021b) for a detailed review), such as adapting the PMW algorithms for better dealing with distinct surface environments (Turk et al., 2021), or correctly filling the gaps between the PMW and IR observation (Tan et al., 2021), which are expected to improve the applicability of SMPPs for landslide applications.

5/ Conclusions

We have analyzed the rainfall during 20 storm events which caused widespread landsliding, as recorded by three rainfall products based (partially or totally) on satellite measurements. Specifically, we have focussed on the recorded rainfall anomaly, that is the maximal rainfall over a given timescale, normalized by the 10-year return rainfall over this same timescale. Though the spatio-temporal pattern of retrieved anomalies varies somewhat from product to product, at least one product coincides, at least partially with the area of widespread landsliding in 11 cases, and the rainfall event which caused landsliding was retrieved as the largest anomalies of the observation period in 12 cases. Typhoons and hurricanes with rainfall lasting several days over large areas are most often retrieved as substantial anomalies, often at the 48h timescale, while landslide events caused by short, localized rainfall seem to be the hardest to retrieve. In any case, we found that using anomalies allows to remove substantial interproduct variability and bias in the absolute estimate of rainfall, and in some cases to better relocate the area with high landslide hazard. Thus we suggest implementing the normalization of the satellite long-term records in an operational landslide hazard awareness algorithm (e.g., Kirschbaum and Stanley, 2018). Still, there is large room for improvement in the satellite product, to better constrain the 10-year rainfall and the rainfall events, possibly by better integrating spatial information from lightning activity and orographic processes, often important in mountainous areas. Also, to improve the operational use of rainfall anomaly, future studies should evaluate how to define anomaly combining early and nowcast products (Otsuka et al., 2016, Kotsuki et al., 2019) with long-term rainfall products to derive extreme climatology, and the impact of the evolution of satellite constellation on the estimation of the 10- or 20-year return rainfall.

Acknowledgments.

The author declares no conflict of interest. We thank Ben Mirus and two anonymous reviewers for constructive comments that helped to clarify and strengthen the paper. We are grateful to E. Zorzetto for distributing his codes to compute the metastatistical extreme value distribution (https://github.com/EnricoZorzetto/mevpy).

Data Availability Statement.

The disaster database information is available at EM-DAT, CRED / UC Louvain, Brussels, Belgium – www.emdat.be (D. Guha-Sapir, last accessed 12/10/2021).

The GPM IMERG Final Precipitation L3 Half Hourly 0.1 degree x 0.1 degree V06B data were obtained from the Goddard Earth Sciences Data and Information Services Center (GES DISC), Greenbelt, MD, https://doi.org/10.5067/GPM/IMERG/3B-HH/06. The GSMaP Gauge Precipitation L3 Hourly 0.1 degree x 0.1 degree V6 data were acquired from https://sharaku.eorc.jaxa.jp/GSMaP/. The MSWEP 3-hourly 0.25° global gridded precipitation V2 data were freely accessed via http://www.gloh2o.org.

The landslide database is accessible through the different work listed in the references.

REFERENCES

van Asch, Th. W. J., J. Buma, and L. P. H. Van Beek, 1999: A view on some hydrological triggering systems in landslides. *Geomorphology*, **30**, 25–32, https://doi.org/10.1016/S0169-555X(99)00042-2.

AghaKouchak, A., A. Behrangi, S. Sorooshian, K. Hsu, and E. Amitai, 2011: Evaluation of satellite-retrieved extreme precipitation rates across the central United States. *Journal of Geophysical Research: Atmospheres*, **116**, https://doi.org/10.1029/2010JD014741.

Amatya, P., D. Kirschbaum, T. Stanley, and H. Tanyas, 2021: Landslide mapping using object-based image analysis and open source tools. *Engineering Geology*, **282**, 106000, https://doi.org/10.1016/j.enggeo.2021.106000.

Aonashi, K., and Coauthors, 2009: GSMaP passive microwave precipitation retrieval algorithm: Algorithm description and validation. J. Meteor. Soc. Japan, 87A, 119–136, https://doi.org/10.2151/jmsj.87A.119

Ardizzone, F., and Coauthors, 2012: Landslide inventory map for the Briga and the Giampilieri catchments, NE Sicily, Italy. *Journal of Maps*, **8**, 176–180, https://doi.org/10.1080/17445647.2012.694271.

Ayat, H.; Evans, J.P.; Behrangi, A. How do different sensors impact IMERG precipitation estimates during hurricane days? Remote Sens. Environ. 2021, 259, 112417.

Battan, L. J., 1965: Some Factors Governing Precipitation and Lightning from Convective Clouds. *Journal of the Atmospheric Sciences*, **22**, 79–84, https://doi.org/10.1175/1520-0469(1965)022<0079:SFGPAL>2.0.CO;2.

Baum, R. L., J. W. Godt, and W. Z. Savage, 2010: Estimating the timing and location of shallow rainfall-induced landslides using a model for transient, unsaturated infiltration. *Journal of Geophysical Research: Earth Surface*, **115**, F03013, https://doi.org/10.1029/2009JF001321.

Beck, H. E., and Coauthors, 2017: Global-scale evaluation of 23 precipitation datasets using gauge observations and hydrological modeling. *Hydrol. Earth Syst. Sci. Discuss.*, **2017**, 1–23, https://doi.org/10.5194/hess-2017-508.

Bogaard, T., and R. Greco, 2018: Invited perspectives: Hydrological perspectives on precipitation intensity-duration thresholds for landslide initiation: proposing hydro-meteorological thresholds. *Natural Hazards and Earth System Sciences*, **18**, 31–39, https://doi.org/10.5194/nhess-18-31-2018.

Brönnimann, C., M. Stähli, P. Schneider, L. Seward, and S. M. Springman, 2013: Bedrock exfiltration as a triggering mechanism for shallow landslides. *Water Resources Research*, **49**, 5155–5167, https://doi.org/10.1002/wrcr.20386.

Brunetti, M. T., M. Melillo, S. Peruccacci, L. Ciabatta, and L. Brocca, 2018: How far are we from the use of satellite rainfall products in landslide forecasting? *Remote Sensing of Environment*, **210**, 65–75, https://doi.org/10.1016/j.rse.2018.03.016.

Coe, J. A., J. W. Kean, J. W. Godt, R. L. Baum, E. S. Jones, D. J. Gochis, and G. S. Anderson, 2014: New insights into debris-flow hazards from an extraordinary event in the Colorado Front Range. *GSAT*, **24**, 4–10, https://doi.org/10.1130/GSATG214A.1.

Chen, Y., K. Chang, H. Lee, and S. Chiang, 2015: Average landslide erosion rate at the watershed scale in southern Taiwan estimated from magnitude and frequency of rainfall. *Geomorphology*, **228**, 756–764, https://doi.org/10.1016/j.geomorph.2014.07.022.

Chen, Y.-C., K. Chang, Y.-J. Chiu, S.-M. Lau, and H.-Y. Lee, 2013: Quantifying rainfall controls on catchment-scale landslide erosion in Taiwan. *Earth Surface Processes and Landforms*, **38**, 372–382, https://doi.org/10.1002/esp.3284.

Chien, F.-C., and H.-C. Kuo, 2011: On the extreme rainfall of Typhoon Morakot (2009). *Journal of Geophysical Research: Atmospheres*, **116**, D05104, https://doi.org/10.1029/2010JD015092.

Davis, C., B. Brown, and R. Bullock, 2006: Object-Based Verification of Precipitation Forecasts. Part I: Methodology and Application to Mesoscale Rain Areas. *Monthly Weather Review*, **134**, 1772–1784, https://doi.org/10.1175/MWR3145.1.

Deprez, A., and Coauthors, 2019: A tailored machine learning method for inventorying landslides from satellite optical imagery. Vol. 21 of, EGU General Assembly Conference, Vienna, 13947 https://ui.adsabs.harvard.edu/abs/2019EGUGA..2113947D (Accessed October 29, 2021).

Dietrich, W. E., R. Reiss, M.-L. Hsu, and D. R. Montgomery, 1995: A process-based model for colluvial soil depth and shallow landsliding using digital elevation data. *Hydrological Processes*, **9**, 383–400, https://doi.org/10.1002/hyp.3360090311.

Elsaesser, G. S., & Kummerow, C. D. (2015). The Sensitivity of Rainfall Estimation to Error Assumptions in a Bayesian Passive Microwave Retrieval Algorithm, Journal of Applied Meteorology and Climatology, 54(2), 408-422.

Emberson, R., D. Kirschbaum, P. Amatya, H. Tanyas, and O. Marc, 2021: Insights from the topographic characteristics of a large global catalog of rainfall-induced landslide event inventories. *Natural Hazards and Earth System Sciences Discussions*, 1–33, https://doi.org/10.5194/nhess-2021-250.

Farahmand, A., and A. AghaKouchak, 2013: A satellite-based global landslide model. *Natural Hazards and Earth System Sciences*, **13**, 1259–1267, https://doi.org/10.5194/nhess-13-1259-2013.

Felsberg, A., G. J. M. D. Lannoy, M. Girotto, J. Poesen, R. H. Reichle, and T. Stanley, 2021: Global soil water estimates as landslide predictor: the effectiveness of SMOS, SMAP and GRACE observations, land surface simulations and data assimilation. *Journal of Hydrometeorology*, **1**, https://doi.org/10.1175/JHM-D-20-0228.1.

Froude, M. J., and D. N. Petley, 2018: Global fatal landslide occurrence from 2004 to 2016. *Natural Hazards and Earth System Sciences*, **18**, 2161–2181, https://doi.org/10.5194/nhess-18-2161-2018.

García-Delgado, H., S. Machuca, and E. Medina, 2019: Dynamic and geomorphic characterizations of the Mocoa debris flow (March 31, 2017, Putumayo Department, southern Colombia). *Landslides*, **16**, 597–609, https://doi.org/10.1007/s10346-018-01121-3.

Goodman, S. J., and Coauthors, 2013: The GOES-R Geostationary Lightning Mapper (GLM). *Atmospheric Research*, **125–126**, 34–49, https://doi.org/10.1016/j.atmosres.2013.01.006.

Guilloteau, C., R. Roca, and M. Gosset, 2016: A Multiscale Evaluation of the Detection Capabilities of High-Resolution Satellite Precipitation Products in West Africa. *Journal of Hydrometeorology*, **17**, 2041–2059, https://doi.org/10.1175/JHM-D-15-0148.1.

Guilloteau, C., Foufoula-Georgiou, E., & Kummerow, C. D. (2017). Global Multiscale Evaluation of Satellite Passive Microwave Retrieval of Precipitation during the TRMM and GPM Eras: Effective Resolution and Regional Diagnostics for Future Algorithm Development, Journal of Hydrometeorology, 18(11), 3051-3070.

Guilloteau, C., Foufoula-Georgiou, E., Kirstetter, P., Tan, J., & Huffman, G. J. (2021). How Well Do Multisatellite Products Capture the Space–Time Dynamics of Precipitation? Part I: Five Products Assessed via a Wavenumber–Frequency Decomposition, Journal of Hydrometeorology, 22(11), 2805-2823.

Guzzetti, F., S. Peruccacci, M. Rossi, and C. P. Stark, 2008: The rainfall intensity–duration control of shallow landslides and debris flows: an update. *Landslides*, **5**, 3–17, https://doi.org/10.1007/s10346-007-0112-1.

Han, S., and P. Coulibaly, 2017: Bayesian flood forecasting methods: A review. *Journal of Hydrology*, **551**, 340–351, https://doi.org/10.1016/j.jhydrol.2017.06.004.

Hartmann, J., & Moosdorf, N, 2012: The new global lithological map database GLiM: A representation of rock properties at the Earth surface. *Geochemistry, Geophysics, Geosystems*, 13(12), 1–37. https://doi.org/10.1029/2012GC004370.

Hong, K.L. Hsu, S. Sorooshian, X. Gao, 2004: Precipitation Estimation from Remotely Sensed Imagery Using an Artificial Neural Network Cloud Classification System. J. Appl. Meteorol., 43, 1834–1852.

Houze Jr., R. A., 2012: Orographic effects on precipitating clouds. *Reviews of Geophysics*, **50**, https://doi.org/10.1029/2011RG000365.

Huang, M. Y.-F., and D. R. Montgomery, 2012: Fluvial response to rapid episodic erosion by earthquake and typhoons, Tachia River, central Taiwan. *Geomorphology*, **175–176**, 126–138, https://doi.org/10.1016/j.geomorph.2012.07.004.

Huffman, G.J., D.T. Bolvin, D. Braithwaite, K. Hsu, R. Joyce, C. Kidd, E.J. Nelkin, S. Sorooshian, J. Tan, P. Xie, 2019: Algorithm Theoretical Basis Document (ATBD) Version 5.2 for the NASA Global Precipitation Measurement (GPM) Integrated Multi-satellitE Retrievals for GPM (I-MERG). GPM Project, Greenbelt, MD, 38 pp. https://pmm.nasa.gov/sites/default/files/document_files/IMERG_ATBD_V6.pdf

Huffman, G.J., R.F. Adler, D.T. Bolvin, E.J. Nelkin, 2010: The TRMM Multi-satellite Precipitation Analysis (TMPA). Chapter 1 in Satellite Rainfall Applications for Surface Hydrology, F. Hossain and M. Gebremichael, Eds. Springer Verlag, ISBN: 978-90-481-2914-0, 3-22.

Huffman, G.J., R.F. Adler, D.T. Bolvin, G. Gu, E.J. Nelkin, K.P. Bowman, Y. Hong, E.F. Stocker, D.B. Wolff, 2007: The TRMM Multi-satellite Precipitation Analysis: QuasiGlobal, Multi-Year, Combined-Sensor Precipitation Estimates at Fine Scale. J. Hydrometeor., 8, 38-55.

Iida, T., 2004: Theoretical research on the relationship between return period of rainfall and shallow landslides. *Hydrological Processes*, **18**, 739–756, https://doi.org/10.1002/hyp.1264.

Iverson, R. M., 2000: Landslide triggering by rain infiltration. *Water Resources Research*, **36**, 1897–1910, https://doi.org/10.1029/2000WR900090.

Joyce, R. J., J. E. Janowiak, P. A. Arkin, and P. Xi, 2004: CMORPH: A method that produces global precipitation estimates from passive microwave and infrared data at high spatial and temporal resolution. J. Hydrometeor., 5, 487–503, https://doi.org/10.1175/1525-7541(2004)005<0487:CAMTPG>2.0.CO;2.

Joyce, R.J., P. Xie, J.E. Janowiak, 2011: Kalman Filter Based CMORPH. J. Hydrometeor., 12, 1547-1563. doi:10.1175/JHM-D-11-022.1

Kato, R., K. Shimose, and S. Shimizu, 2018: Predictability of Precipitation Caused by Linear Precipitation Systems During the July 2017 Northern Kyushu Heavy Rainfall Event Using a Cloud-Resolving Numerical Weather Prediction Model. *Journal of Disaster Research*, **13**, 846–859, https://doi.org/10.20965/jdr.2018.p0846.

Kidd, C., Matsui, T., Chern, J., Mohr, K., Kummerow, C.D. and Randel, D. (2015) Precipitation estimates from cross-track passive microwave observations using a physically based retrieval scheme. Journal of Hydrometeorology, 17, 383– 400. https://doi.org/10.1175/JHM-D-15-0051.1

Kidd, C., Matsui, T. and S. Ringerud, S (2021a) Precipitation Retrievals from Passive Microwave Cross-Track Sensors: The Precipitation Retrieval and Profiling Scheme. Remote Sens. 13, 947. https://doi.org/10.3390/rs13050947

Kidd, C., Huffman, G., Maggioni, V., Chambon, P., & Oki, R. (2021b). The Global Satellite Precipitation Constellation: Current Status and Future Requirements, Bulletin of the American Meteorological Society, 102(10), E1844-E1861

Kidd, C., Tan, J., Kirstetter, P., Petersen, W.A. Validation of the version 05 level 2 precipitation products from the GPM Core Observatory and constellation satellite sensors Q. J. R. Meteorol. Soc., 144 (2018), pp. 313-328, 10.1002/qj.3175.

Kirschbaum, D., and T. Stanley, 2018: Satellite-Based Assessment of Rainfall-Triggered Landslide Hazard for Situational Awareness. *Earth's Future*, **6**, 505–523, https://doi.org/10.1002/2017EF000715.

Kirschbaum, D., S. B. Kapnick, T. Stanley, and S. Pascale, 2020: Changes in Extreme Precipitation and Landslides Over High Mountain Asia. *Geophysical Research Letters*, **47**, e2019GL085347, https://doi.org/10.1029/2019GL085347.

Kirschbaum, D. B., R. Adler, Y. Hong, and A. Lerner-Lam, 2009: Evaluation of a preliminary satellite-based landslide hazard algorithm using global landslide inventories. *Nat. Hazards Earth Syst. Sci.*, **9**, 673–686, https://doi.org/10.5194/nhess-9-673-2009.

——, T. Stanley, and J. Simmons, 2015: A dynamic landslide hazard assessment system for Central America and Hispaniola. *Natural Hazards and Earth System Sciences*, **15**, 2257–2272, https://doi.org/10.5194/nhess-15-2257-2015.

Kondo K., Numamoto S., and Hayashi S., 2004: Disasters due to slope failures caused by Typhoon Meari (T0421) in Miyagawa village, Mie Prefecture. *Journal of the Japan Landslide Society*, **41**, 419–422, https://doi.org/10.3313/jls.41.4_419.

Kottek, M., J. Grieser, C. Beck, B. Rudolf, and F. Rubel, 2006: World Map of the Köppen-Geiger climate classification updated. *Meteorologische Zeitschrift*, 259–263, https://doi.org/10.1127/0941-2948/2006/0130.

Kotsuki, S., K. Kurosawa, S. Otsuka, K. Terasaki, and T. Miyoshi, 2019: Global Precipitation Forecasts by Merging Extrapolation-Based Nowcast and Numerical Weather Prediction with Locally Optimized Weights. *Weather and Forecasting*, **34**, 701–714, https://doi.org/10.1175/WAF-D-18-0164.1.

Kubota, T., K. Aonashi, T. Ushio, S. Shige, Y. N. Takayabu, M. Kachi, Y. Arai, T. Tashima, T. Masaki, N. Kawamoto, T. Mega, M. K. Yamamoto, A. Hamada, M. Yamaji, G. Liu, and R. Oki, 2020: Global Satellite Mapping of Precipitation (GSMaP) products in the GPM era. Satellite Precipitation Measurement. Levizzani, V., C. Kidd, D. B. Kirschbaum, C. D. Kummerow, K. Nakamura, and F. J. Turk (eds.), Springer, Cham, Advances in Global Change Research, 67, 355–373.

Kubota, T., S. Shige, H. Hashizume, K. Aonashi, N. Takahashi, S. Seto, M. Hirose, Y. N. Takayabu, T. Ushio, K. Nakagawa, K. Iwanami, M. Kachi, and K. Okamoto, 2007: Global precipitation map using satellite-borne microwave radiometers by the GSMaP project: Production and validation. IEEE Trans. Geosci. Remote Sens., 45, 2259–2275.

Kummerow, C. D., D. L. Randel, M. Kulie, N.-Y. Wang, R. Ferraro, S. Joseph Munchak, and V. Petkovic, 2015: The evolution of the Goddard profiling algorithm to a fully parametric scheme. J. Atmos. Oceanic Technol., 32, 2265–2280, https://doi.org/10.1175/JTECH-D-15-0039.1.

Lacerda, W. A., 1997: STABILITY OF NATURAL SLOPES ALONG THE TROPICAL COAST OF BRAZIL. https://trid.trb.org/view/476474 (Accessed February 18, 2021).

Lin, G.-W., H. Chen, N. Hovius, M.-J. Horng, S. Dadson, P. Meunier, and M. Lines, 2008: Effects of earthquake and cyclone sequencing on landsliding and fluvial sediment transfer in a mountain catchment. *Earth Surface Processes and Landforms*, **33**, 1354–1373, https://doi.org/10.1002/esp.1716.

Mahrooghy, M., V. G. Anantharaj, N. H. Younan, W. A. Petersen, K.-L. Hsu, A. Behrangi, and J. Aanstoos, 2013: Augmenting satellite precipitation estimation with lightning information. *International Journal of Remote Sensing*, **34**, 5796–5811, https://doi.org/10.1080/01431161.2013.796100.

Marc, O., N. Hovius, P. Meunier, T. Uchida, and S. Hayashi, 2015: Transient changes of landslide rates after earthquakes. *Geology*, **43**, 883–886, https://doi.org/10.1130/G36961.1.

Marc, O., A. Stumpf, J.-P. Malet, M. Gosset, T. Uchida, and S.-H. Chiang, 2018: Initial insights from a global database of rainfall-induced landslide inventories: the weak influence of slope and strong influence of total storm rainfall. *Earth Surface Dynamics*, **6**, 903–922, https://doi.org/10.5194/esurf-6-903-2018.

——, M. Gosset, H. Saito, T. Uchida, and J.-P. Malet, 2019: Spatial Patterns of Storm-Induced Landslides and Their Relation to Rainfall Anomaly Maps. *Geophysical Research Letters*, **46**, 11167–11177, https://doi.org/10.1029/2019GL083173.

Marra, F., E. I. Nikolopoulos, E. N. Anagnostou, and E. Morin, 2018: Metastatistical Extreme Value analysis of hourly rainfall from short records: Estimation of high quantiles and impact of measurement errors. Advances in Water Resources, 117, 27–39, https://doi.org/10.1016/j.advwatres.2018.05.001.

Marra, F., M. Borga, and E. Morin, 2020: A Unified Framework for Extreme Subdaily Precipitation Frequency Analyses Based on Ordinary Events. *Geophysical Research Letters*, **47**, e2020GL090209, https://doi.org/10.1029/2020GL090209.

Mega, T., T. Ushio, M. Takahiro, T. Kubota, M. Kachi, and R. Oki, 2019: Gauge-Adjusted Global Satellite Mapping of Precipitation. *IEEE Transactions on Geoscience and Remote Sensing*, **57**, 1928–1935, https://doi.org/10.1109/TGRS.2018.2870199.

Mehran, A., and A. AghaKouchak, 2014: Capabilities of satellite precipitation datasets to estimate heavy precipitation rates at different temporal accumulations. *Hydrological Processes*, **28**, 2262–2270, https://doi.org/10.1002/hyp.9779.

Meunier, P., N. Hovius, and A. J. Haines, 2007: Regional patterns of earthquake-triggered landslides and their relation to ground motion. *Geophysical Research Letters*, **34**, L20408, https://doi.org/10.1029/2007GL031337.

Minjarez-Sosa, C. M., and J. Waissman, 2017: A Survey and Perspectives on Mathematical Models for Quantitative Precipitation Estimation Using Lightning. *Advances in Meteorology*, https://doi.org/10.1155/2017/1351308.

Mondini, A. C., 2017: Measures of Spatial Autocorrelation Changes in Multitemporal SAR Images for Event Landslides Detection. *Remote Sensing*, **9**, 554, https://doi.org/10.3390/rs9060554.

Netto, A. L. C., and Coauthors, 2013: January 2011: The Extreme Landslide Disaster in Brazil. Landslide Science and Practice, Springer, Berlin, Heidelberg, 377–384.

Nikolopoulos, E. I., E. Destro, V. Maggioni, F. Marra, and M. Borga, 2017: Satellite Rainfall Estimates for Debris Flow Prediction: An Evaluation Based on Rainfall Accumulation–Duration Thresholds. *Journal of Hydrometeorology*, **18**, 2207–2214, https://doi.org/10.1175/JHM-D-17-0052.1.

Oliveira, R.; Maggioni, V.; Vila, D.; Morales, C. Characteristics and Diurnal Cycle of GPM Rainfall Estimates over the Central Amazon Region. Remote Sens. 2016, 8, 544. https://doi.org/10.3390/rs8070544

Otsuka, S., S. Kotsuki, and T. Miyoshi, 2016: Nowcasting with Data Assimilation: A Case of Global Satellite Mapping of Precipitation. *Weather and Forecasting*, **31**, 1409–1416, https://doi.org/10.1175/WAF-D-16-0039.1.

Ozturk, U., H. Saito, Y. Matsushi, I. Crisologo, and W. Schwanghart, 2021: Can global rainfall estimates (satellite and reanalysis) aid landslide hindcasting? *Landslides*, https://doi.org/10.1007/s10346-021-01689-3.

Petley, D., 2012: Global patterns of loss of life from landslides. *Geology*, **40**, 927–930, https://doi.org/10.1130/G33217.1.

Piepgrass, M. V., E. P. Krider, and C. B. Moore, 1982: Lightning and surface rainfall during Florida thunderstorms. *Journal of Geophysical Research: Oceans*, **87**, 11193–11201, https://doi.org/10.1029/JC087iC13p11193.

Prancevic, J. P., M. P. Lamb, B. W. McArdell, C. Rickli, and J. W. Kirchner, 2020: Decreasing Landslide Erosion on Steeper Slopes in Soil-Mantled Landscapes. *Geophysical Research Letters*, **47**, e2020GL087505, https://doi.org/10.1029/2020GL087505.

Reiser, H., and H. Kutiel, 2009: Rainfall uncertainty in the Mediterranean: definitions of the daily rainfall threshold (DRT) and the rainy season length (RSL). *Theor Appl Climatol*, **97**, 151–162, https://doi.org/10.1007/s00704-008-0055-z.

Roberts, N. M., and H. W. Lean, 2008: Scale-Selective Verification of Rainfall Accumulations from High-Resolution Forecasts of Convective Events. *Monthly Weather Review*, **136**, 78–97, https://doi.org/10.1175/2007MWR2123.1.

Roca, R., Chambon, P., Jobard, I., Kirstetter, P.-E., Gosset, M., Bergès, G. C. Comparing satellite and surface rainfall products over West Africa at meteorologically relevant scales during the AMMA campaign using error estimates. Journal of Applied Meteorology and Climatology, American Meteorological Society, 2010, 49 (4), pp.715-731. ff10.1175/2009JAMC2318.1

Rossi, M., S. Luciani, D. Valigi, D. Kirschbaum, M. T. Brunetti, S. Peruccacci, and F. Guzzetti, 2017: Statistical approaches for the definition of landslide rainfall thresholds and their uncertainty using rain gauge and satellite data. *Geomorphology*, **285**, 16–27, https://doi.org/10.1016/j.geomorph.2017.02.001.

Rosso, R., M. C. Rulli, and G. Vannucchi, 2006: A physically based model for the hydrologic control on shallow landsliding. *Water Resources Research*, **42**, https://doi.org/10.1029/2005WR004369.

von Ruette, J., P. Lehmann, and D. Or, 2014: Effects of rainfall spatial variability and intermittency on shallow landslide triggering patterns at a catchment scale. *Water Resources Research*, **50**, 7780–7799, https://doi.org/10.1002/2013WR015122.

Saito, H., and H. Matsuyama, 2012: Catastrophic Landslide Disasters Triggered by Record-Breaking Rainfall in Japan: Their Accurate Detection with Normalized Soil Water Index in the Kii Peninsula for the Year 2011. *Sola*, **8**, 81–84, https://doi.org/10.2151/sola.2012-021.

Saito, H., and H. Matsuyama, 2015: Probable Hourly Precipitation and Soil Water Index for 50-yr Recurrence Interval over the Japanese Archipelago. *SOLA*, **11**, 118–123, https://doi.org/10.2151/sola.2015-028.

——, O. Korup, T. Uchida, S. Hayashi, and T. Oguchi, 2014: Rainfall conditions, typhoon frequency, and contemporary landslide erosion in Japan. *Geology*, **42**, 999–1002, https://doi.org/10.1130/G35680.1.

Shige, S., S. Kida, H. Ashiwake, T. Kubota, and K. Aonashi, 2012: Improvement of TMI Rain Retrievals in Mountainous Areas. *Journal of Applied Meteorology and Climatology*, **52**, 242–254, https://doi.org/10.1175/JAMC-D-12-074.1.

Shuin, Y., N. Hotta, M. Suzuki, and K. Ogawa, 2012: Estimating the effects of heavy rainfall conditions on shallow landslides using a distributed landslide conceptual model. *Physics and Chemistry of the Earth, Parts A/B/C*, **49**, 44–51, https://doi.org/10.1016/j.pce.2011.06.002.

Soula, S., and S. Chauzy, 2001: Some aspects of the correlation between lightning and rain activities in thunderstorms. *Atmospheric Research*, **56**, 355–373, https://doi.org/10.1016/S0169-8095(00)00086-7.

Stanley, T. A., D. B. Kirschbaum, G. Benz, R. A. Emberson, P. M. Amatya, W. Medwedeff, and M. K. Clark, 2021: Data-Driven Landslide Nowcasting at the Global Scale. *Frontiers in Earth Science*, **9**.

Stumpf, A., N. Lachiche, J.-P. Malet, N. Kerle, and A. Puissant, 2014: Active Learning in the Spatial Domain for Remote Sensing Image Classification. *IEEE Transactions on Geoscience and Remote Sensing*, **52**, 2492–2507, https://doi.org/10.1109/TGRS.2013.2262052.

Tan, J., Huffman, G. J., Bolvin, D. T., Nelkin, E. J., & Rajagopal, M., 2021: SHARPEN: A Scheme to Restore the Distribution of Averaged Precipitation Fields, Journal of Hydrometeorology, 22(8), 2105-2116.

Tan, J., Petersen, W. A., & Tokay, A. (2016). A Novel Approach to Identify Sources of Errors in IMERG for GPM Ground Validation, Journal of Hydrometeorology, 17(9), 2477-2491

Tan, J., Petersen, W. A., Kirchengast, G., Goodrich, D. C., & Wolff, D. B., 2018: Evaluation of Global Precipitation Measurement Rainfall Estimates against Three Dense Gauge Networks, Journal of Hydrometeorology, 19(3), 517-532.

Thomas, M. A., B. B. Mirus, and B. D. Collins, 2018: Identifying Physics-Based Thresholds for Rainfall-Induced Landsliding. *Geophysical Research Letters*, **45**, 9651–9661, https://doi.org/10.1029/2018GL079662.

——, B. D. Collins, and B. B. Mirus, 2019: Assessing the Feasibility of Satellite-Based Thresholds for Hydrologically Driven Landsliding. *Water Resources Research*, **55**, 9006–9023, https://doi.org/10.1029/2019WR025577.

Turk, F. J., Ringerud, S. E., You, Y., Camplani, A., Casella, D., Panegrossi, G., Sanò, P., Ebtehaj, A., Guilloteau, C., Utsumi, N., Prigent, C., and C. Peters-Lidard, 2021: Adapting Passive Microwave-Based Precipitation Algorithms to Variable Microwave Land Surface Emissivity to Improve Precipitation Estimation from the GPM Constellation, *Journal of Hydrometeorology*, 22(7), 1755-1781.

UNOSAT, 2016, Dominica Landslides TS Erika, http://charim-geonode.net/layers/geonode:landslides_unosat3, last accessed Nov 2021.

Ushio, T., K. Sasashige, T. Kubota, S. Shige, K. Okamoto, K. Aonashi, T. Inoue, N. Takahashi, T. Iguchi, M. Kachi, R. Oki, T. Morimoto, and Z. Kawasaki, 2009: A Kalman filter approach to the Global Satellite Mapping of Precipitation (GSMaP) from combined passive microwave and infrared radiometric data. *J. Meteor. Soc. Japan*, 87A, 137–151.

Wang, F., Y.-H. Wu, H. Yang, Y. Tanida, and A. Kamei, 2015: Preliminary investigation of the 20 August 2014 debris flows triggered by a severe rainstorm in Hiroshima City, Japan. *Geoenvironmental Disasters*, **2**, 17, https://doi.org/10.1186/s40677-015-0025-6.

Wang, G., A. Suemine, G. Furuya, M. Kaibori, and K. Sassa, 2005: Rainstorm-induced landslides at Kisawa village, Tokushima Prefecture, Japan, August 2004. *Landslides*, **2**, 235–242, https://doi.org/10.1007/s10346-005-0061-5.

Watakabe, T., and Y. Matsushi, 2019: Lithological controls on hydrological processes that trigger shallow landslides: Observations from granite and hornfels hillslopes in Hiroshima, Japan. *CATENA*, **180**, 55–68, https://doi.org/10.1016/j.catena.2019.04.010.

van Westen, C. J., and J., Zhang, 2018: Landslides and floods triggered by Huricane Maria (18 September, 2017) in Dominica. Digital or Visual Products, UNITAR-UNOSAT . http://www.unitar.org/unosat/node/44/2762, last accessed Nov. 2021.

Wilson, R. C., and G. F. Wieczorek, 1995: Rainfall Thresholds for the Initiation of Debris Flows at La Honda, California. *Environmental & Engineering Geoscience*, **I**, 11–27, https://doi.org/10.2113/gseegeosci.I.1.11.

Wu, W., R. Emerton, Q. Duan, A. W. Wood, F. Wetterhall, and D. E. Robertson, 2020: Ensemble flood forecasting: Current status and future opportunities. *WIREs Water*, **7**, e1432, https://doi.org/10.1002/wat2.1432.

Xu, W., R. F. Adler, and N.-Y. Wang, 2013: Improving Geostationary Satellite Rainfall Estimates Using Lightning Observations: Underlying Lightning–Rainfall–Cloud Relationships. *Journal of Applied Meteorology and Climatology*, **52**, 213–229, https://doi.org/10.1175/JAMC-D-12-040.1.

Yamamoto, M. K., S. Shige, C.-K. Yu, and L.-W. Cheng, 2017: Further improvement of the heavy orographic rainfall retrievals in the GSMaP algorithm for microwave radiometers. *Journal of Applied Meteorology and Climatology*, https://doi.org/10.1175/JAMC-D-16-0332.1.

You, Y., Petkovic, V., Tan, J., Kroodsma, R., Berg, W., Kidd, C., and C., Peters-Lidard, 2020a: Evaluation of V05 Precipitation Estimates from GPM Constellation Radiometers Using KuPR as the Reference, *Journal of Hydrometeorology*, 21(4), 705-728.

You, Y., Wang, N., Kubota, T., Aonashi, K., Shige, S., Kachi, M., Kummerow, C., Randel, D., Ferraro, R., Braun, S., and Y., Takayabu, 2020b: Comparison of TRMM Microwave Imager Rainfall Datasets from NASA and JAXA, *Journal of Hydrometeorology*, 21(3), 377-397.

Zorzetto, E., G. Botter, and M. Marani, 2016: On the emergence of rainfall extremes from ordinary events. *Geophysical Research Letters*, **43**, 8076–8082, https://doi.org/10.1002/2016GL069445.